CHEMISTRY OF MATERIALS

Suppressing Dissolution of Vanadium from Cation-Disordered Li$_{2-x}$VO$_2$F via a Concentrated Electrolyte Approach

Musa Ali Cambaz,[†] Bhaghavathi P. Vinayan,[†] Syed Atif Pervez,[†] Rune E. Johnsen,[‡] Holger Geßwein,[§] Alexander A. Guda,[‖] Yury V. Rusalev,[‖] Michael Kiarie Kinyanjui,[⊥] Ute Kaiser,[⊥] and Maximilian Fichtner*,[†,#]

[†]Helmholtz Institute Ulm (HIU) Electrochemical Energy Storage, Helmholtzstrasse 11, D-89081 Ulm, Germany

[‡]Technical University of Denmark, Department of Energy Conversion and Storage, Frederiksborgvej 399, DK-4000 Roskilde, Denmark

[§]Institute for Applied Materials, Karlsruhe Institute of Technology, Herrmann-von-Helmholtz-Platz 1, D-76344 Eggenstein-Leopoldshafen, Germany

[‖]The Smart Materials Research Institute, Southern Federal University, Sladkova 178/24, 344090 Rostov-on-Don, Russia

[⊥]Central Facility of Electron Microscopy, Ulm University, Albert Einstein Allee 11, 89068 Ulm, Germany

[#]Institute of Nanotechnology, Karlsruhe Institute of Technology, D-76344 Eggenstein-Leopoldshafen, Germany

S *Supporting Information*

ABSTRACT: Li$_2$VO$_2$F with the cation-disordered rock-salt structure is an attractive high-energy-density positive electrode material but suffers from severe capacity fading upon cycling. The underlying reasons are yet unclear. In this study, we unveil the overlooked role of vanadium dissolution and electrode−electrolyte interactions and provide insight into the failure mechanism. Interfacial reactions, in general, can be tuned by either surface coatings or the modification of the electrolyte chemistry. Here we modify the interfacial reactions through the use of a concentrated electrolyte 5.5 M LiFSI in dimethyl carbonate (1:2.16 molar ratio salt to solvent), effectively reducing vanadium dissolution. Moreover, it results in a lower interfacial resistance build-up as compared to conventional 1.0 M LiPF$_6$ electrolyte, thus increasing the cycling stability. The solubility of vanadium enhances significantly with higher oxidation states. Furthermore, a chemical prelithiation strategy has been presented, which allows the full lithiation of VO$_2$F to Li$_2$VO$_2$F, with an outlook on the intermediate phases. We argue that the optimization of cathode−electrolyte interactions is of significant importance to improve the cycling performance of disordered rock-salts, where a thorough understanding of the limiting factors is still missing.
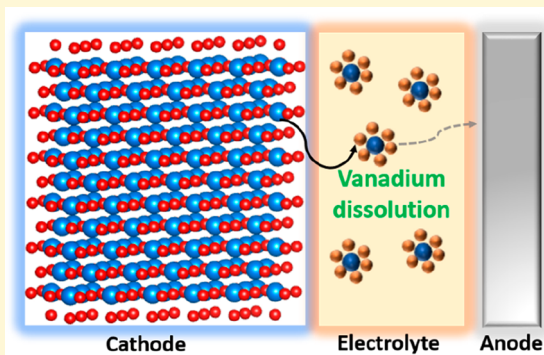
INTRODUCTION

Improving the energy density of rechargeable batteries is one of the core objectives in the energy storage field. It is debatable that the positive electrode material is the bottleneck to improve the specific energy of lithium-ion batteries. State-of-the-art layered rock-salt oxides such as LiCoO$_2$ and LiNi$_{1/3}$Mn$_{1/3}$Co$_{1/3}$O$_2$ exhibit stable specific capacities between 145−165 mAh g^{-1} but practically could not exceed specific capacities higher than 200 mAh g^{-1} with high cycling stability.[1−3] With the discovery of facilitated lithium diffusion in Li-rich disordered rock-salts, this class of compound has evolved into a potential high-capacity cathode material.[4] This finding has opened a new perspective in the search for cathode materials showing only minor or no cation mixing. The chemical space for the cathode design, which is traditionally dominated by Ni-, Mn-, and Co-based oxides, has been broadened. Today already a large number of high capacity positive electrode materials with disordered rock-salt structure have been reported.[5−8] The commonly pursued approach comprises the formation of a hypothetical solid-solution between a divalent or trivalent transition metal with a high-valent charge compensator. These include Ti^{4+},[9] Zr^{4+},[10] Sb^{5+},[11] Nb^{5+},[12] and Mo^{6+6} where the transition metal is anticipated to be electrochemically inactive. Nevertheless, oxygen redox can partially reverse this penalty by contributing to the overall capacity beyond the transition metal redox capacity. This method exhibits two disadvantages: one is a heavier framework structure leading to lower specific capacity, and second, the introduced transition metal offers no redox capacity or is active in an impractical voltage window. An alternative approach is
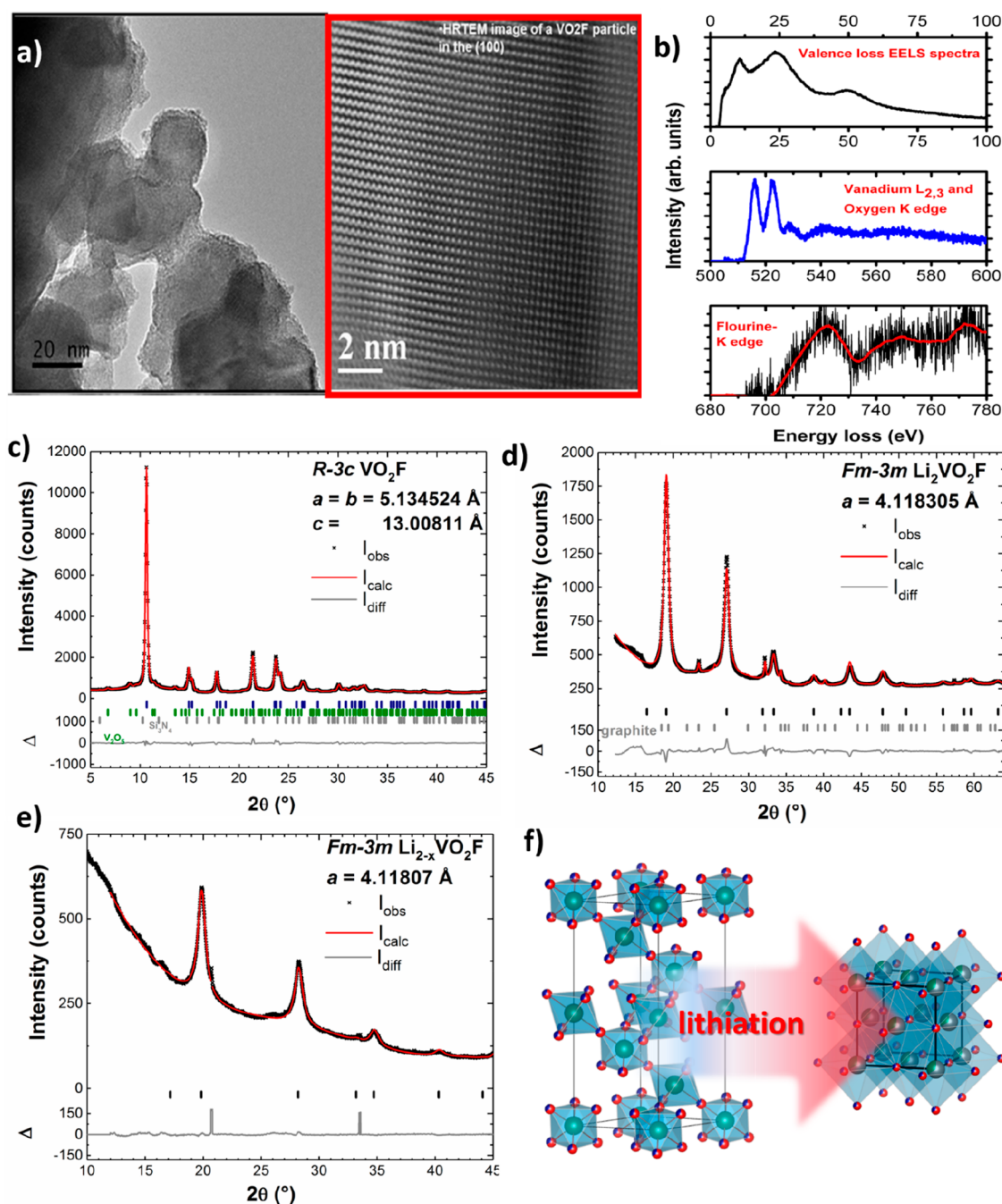
A

Figure 1. (a) HRTEM images of VO_2F with an inset along the [001] zone axis. (b) EELS of VO_2F with valence loss region, overlapped vanadium $L_{2,3}$ edge, and oxygen K-edge, fluorine K-edge. (c) Synchrotron XRPD for rhombohedral VO_2F ($R\overline{3}c$). (d) Synchrotron XRPD for cubic Li_2VO_2F ($Fm\overline{3}m$) carbon composite. (e) XRPD for cubic $Li_{2-x}VO_2F$ ($Fm\overline{3}m$). (f) Schematic illustration of the crystal structures for rhombohedral VO_2F and cubic Li_2VO_2F.[30]

based on the use of transition metals suitable for multiple electron transfers, such as $V^{+3/+5}$,[13,14] $Cr^{3+/5+}$,[15] and $Mo^{3+/6+}$,[16] which exhibit lower average potentials. Attempts to increase the average voltage by introducing an additional transition metal with high voltage redox-couples have shown limited success. On the contrary to layered rock-salt and spinel compounds, the unusual distribution of local cation environments in disordered rock-salts gives rise to the substitution of high levels of oxygen by fluorine.[17] Anion substitution has been shown to increase the average voltage of these oxyfluoride materials in some cases. Hereby, the average oxidation state decreases (for example $Li_2M^{4+}O_3/Li_2M^{3+}O_2F$), which can mitigate oxygen release by increasing the cationic charge reservoir.[18] Substitution of O^{2-} with F^- can be used to introduce lithium-excess (for example $LiM^{3+}O_2/Li_2M^{3+}O_2F$) as an alternative approach to the conventional high-valent doping with heavy, redox-inactive elements and therefore offers higher theoretical capacities. Although new materials and design concepts have been introduced, high cycling stability with minor capacity fading yet has to be demonstrated. Approaches aiming to maximize the transition metal redox capacity by employing multielectron redox couples, in order to
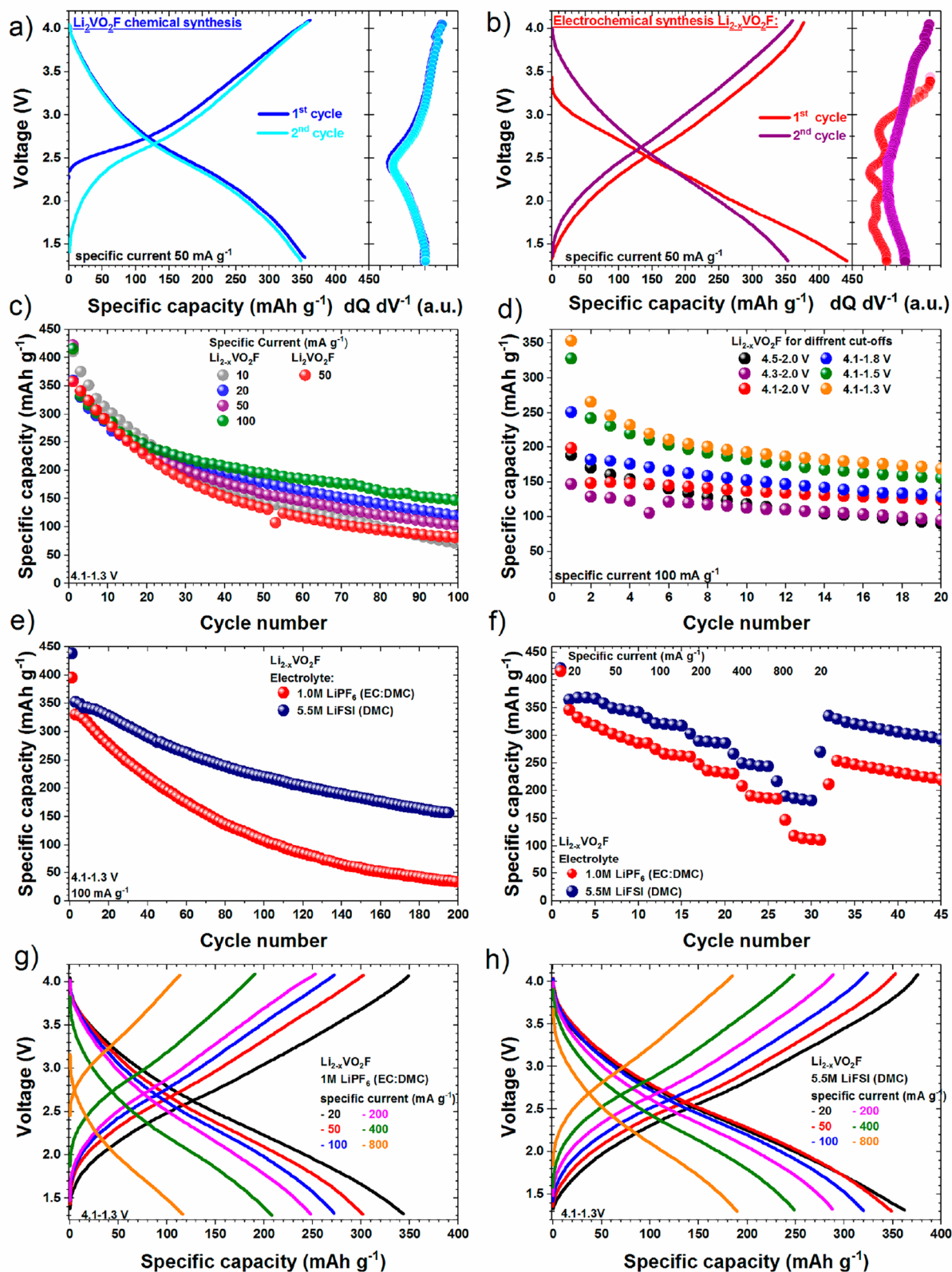
Figure 2. Cycling measurements were conducted in the voltage between 4.1 and 1.3 V unless stated otherwise. Charge–discharge profile of (a) Li_2VO_2F and (b) $Li_{2−x}VO_2F$ at 20 mA g^{-1} with corresponding dQ dV^{-1}. (c) Cycling stability for various specific currents. (d) Cycling stability of $Li_{2−x}VO_2F$ for different cut-offs. (e) Cycling stability of $Li_{2−x}VO_2F$ at 100 mA g^{-1} for 1.0M-LiPF$_6$ and 5.5M-LiFSI. (f) Rate capability test for $Li_{2−x}VO_2F$ for 1.0M-LiPF$_6$ and 5.5M-LiFSI. Respective charge–discharge profile from rate capability test at different specific currents for (g) 1.0M-LiPF$_6$ and (h) 5.5M-LiFSI.

avoid oxygen redox with irreversible O_2 gas release, can be considered as promising.

Li_2VO_2F with a disordered rock-salt structure has a theoretical capacity of 462 mAh g^{-1} based on a 2 electron reaction ($V^{3+/5+}$ redox reaction).[13,14,19−21]The thermal instability of Li_2VO_2F (decomposition >250 °C) imposes challenges in the synthesis and modification of the material.[19] Li_2VO_2F has been synthesized by a direct mechanochemical synthesis route and through electrochemical lithiation of rhombohedral VO_2F perovskite accompanied by an irreversible phase transition to the cubic disordered rock-salt $Li_{2-x}VO_2F$ end phase. Li_2VO_2F is an attractive high-energy-density positive electrode material, but according to recent reports[21,22] suffers from severe capacity fading upon cycling. The reasons for the capacity fade were still unclear. From our earlier work on VO_2F,[13] vanadium deposition was found on the anode and speculated to be a source for capacity degradation. There are a variety of possible side reactions of positive electrode materials; acid−base interactions with HF and PF_5(strong Lewis acid), which are inevitably present or were formed with $LiPF_6$ electrolytes, can lead to metal dissolution.[23] LiFSI salt is chemically more stable as compared to conventional $LiPF_6$ and promises to alleviate these side reactions.[24]

In this work, we focus our efforts on the critical aspect of the electrode−electrolyte interaction of $Li_{2-x}VO_2F$, in order to better understand the degradation mechanism and the influence of the electrolyte thereof. We have used a concentrated 5.5 M LiFSI dimethyl carbonate (DMC) electrolyte (1:2.16 molar ratio salt to solvent)[25,26] and compared it to standard 1 M $LiPF_6$ in DMC and ethylene carbonate (EC) electrolyte. The influence of the electrolyte on the cycling performance of $Li_{2-x}VO_2F$ has been elaborated. X-ray photoelectron spectroscopy (XPS) and electrochemical impedance spectroscopy (EIS) were used in order to chemically and electrochemically analyze the interfaces of the electrodes. Complementary to XPS, Raman mapping was conducted at the anode side to investigate and map the metal deposition. The dissolution of vanadium from the positive electrode for both electrolytes has been compared and quantified for different states of charges. Structural changes and the charge-compensation mechanism have been investigated by X-ray diffraction and absorption methods. Evolving gaseous products during cycling were investigated by differential electrochemical mass spectrometry (DEMS).

■ RESULTS AND DISCUSSION

Synthesis and Characterization. For the electrochemical lithiation of VO_2F to $Li_{2-x}VO_2F$, cells have been constructed and then discharged to 1.3 V versus Li/Li$^+$ at 20 mA g^{-1} current, exhibiting a discharge capacity of 450 mAh g^{-1}, which corresponds to 1.7 Li per formula unit. The synthesis of $R\bar{3}c$ VO_2F has been adopted from our previous work.[13] In the literature,[21] the electrochemical lithiation up to 1.75 Li per f.u. has been reported for the first discharge, similarly to our finding of 1.7 Li per f.u. Hence, the question about the ability to reach full lithiation remained. Here we show the accessibility up to 2 Li per f.u. is possible by chemical lithiation with the reducing agent n-butyllithium (nBuLi) with a relative reduction potential of ∼1.0 V vs Li$^+$/Li^0.[27] The electrochemically synthesized compound will be noted as $Li_{2-x}VO_2F$ due to the off-stoichiometry, and the chemically synthesized will be noted as Li_2VO_2F. The high-resolution transmission electron microscopy (HRTEM) image of VO_2F along the [001] zone

axis with an overview is shown in Figure 1a and reveals the typical morphology for mechanochemically synthesized compounds, showing larger agglomerated particles composed of smaller grains.[28,29] The individual particles are in the range of 20−50 nm. All elements V, O, and F are present, with the vanadium being in the +5 oxidation state, as shown by electron energy loss spectroscopy (EELS) in Figure 1b. The XRPD pattern of the pristine VO_2F with a rhombohedral structure (space group $R\bar{3}c$) is presented in Figure 1c. The refined lattice parameters are $a = b = 5.1345(3)$ Å, $c = 13.008(1)$ Å and volume $V = 296.99(4)$ Å^3. The X-ray powder diffraction (XRPD) of Li_2VO_2F and $Li_{2-x}VO_2F$ are shown in Figures 1d, e, respectively. Both compounds are refined in the cubic disordered rock-salt-type structure with the $Fm\bar{3}m$ space group. The refined lattice parameter for Li_2VO_2F is $a = 4.1183(6)$ Å, and that for $Li_{2-x}VO_2F$ is $a = 4.1180(26)$ Å. The lattice parameters deviate slightly due to the differences in composition. Figure 1f shows the schematic transition of the crystal structure from the rhombohedral VO_2F to the cubic Li_2VO_2F. In the case of the chemically lithiated $Li_{2-x}VO_2F$, a 12 h immersion time led to a mixture of intermediate hexagonal phases and the cubic cation-disordered phase, which is shown in Figure S1 and the lattice parameter are given in Table S1.

Electrochemistry. We compared the electrochemical properties of Li_2VO_2F and $Li_{2-x}VO_2F$. The compounds were tested in the voltage range of 1.3−4.1 V at 20 mA g^{-1} current density. It is important to note that a 2e$^-$ transfer corresponds to a specific capacity of 463 mAh g^{-1} for Li_2VO_2F and to 526 mAh g^{-1} for VO_2F ($Li_{2-x}VO_2F$) due to the lighter framework. For the first discharge, Li_2VO_2F exhibited a specific capacity of 355 mAh g^{-1} (1.53 Li per f.u.) with a sloping voltage profile, as shown in Figure 2a. The corresponding differential capacity versus voltage plots shows a broad peak centered at 2.5 V. Figure 2b shows the first discharge of VO_2F, exhibiting a specific capacity of 440 mAh g^{-1} (1.67 Li per f.u.). The first cycle shows a comparably high irreversible capacity, which we observed already in our previous work on the delithiation of rhombohedral Li_xVO_2F.[13] A closer look at the corresponding differential capacity $(dQ\ dV^{-1})$ versus V plot shows several peaks for the first discharge but only one peak for the consecutive cycles. This can be attributed to the irreversible, rhombohedral to cubic phase transition during the first cycle. For the second cycle, both compounds show a similar sloping voltage profile centered at ∼2.5 V, indicating the chemical similarity of both compounds. Figure 2c shows the cycling stability for different specific currents at 10, 20, 50, and 100 mA g^{-1} for $Li_{2-x}VO_2F$ and at 50 mA g^{-1} for Li_2VO_2F. $Li_{2-x}VO_2F$ shows for the same current density better cycling stability. It is noteworthy that the capacity retention is lower for slower cycling and increases with the current density. This could hint at a chemical instability of the material when in contact with the electrolyte, as lower rates mean longer contact times. Figure 2d shows the cycling stability for various cutoff voltages at 100 mAh g^{-1}. The voltage window limits the governing redox reactions and, therefore, the amount of inserted/extracted lithium. The voltage window has been varied systematically by fixing either the upper cutoff to 4.1 V or the lower cutoff and gradually changing the window. In this respect, lowering the cutoff increases the specific discharge capacity drastically due to the sloping profile. On the contrary, increasing the upper cutoff from 4.1 to 4.5 V also enhances the capacity fading. The capacity retention decreases for higher
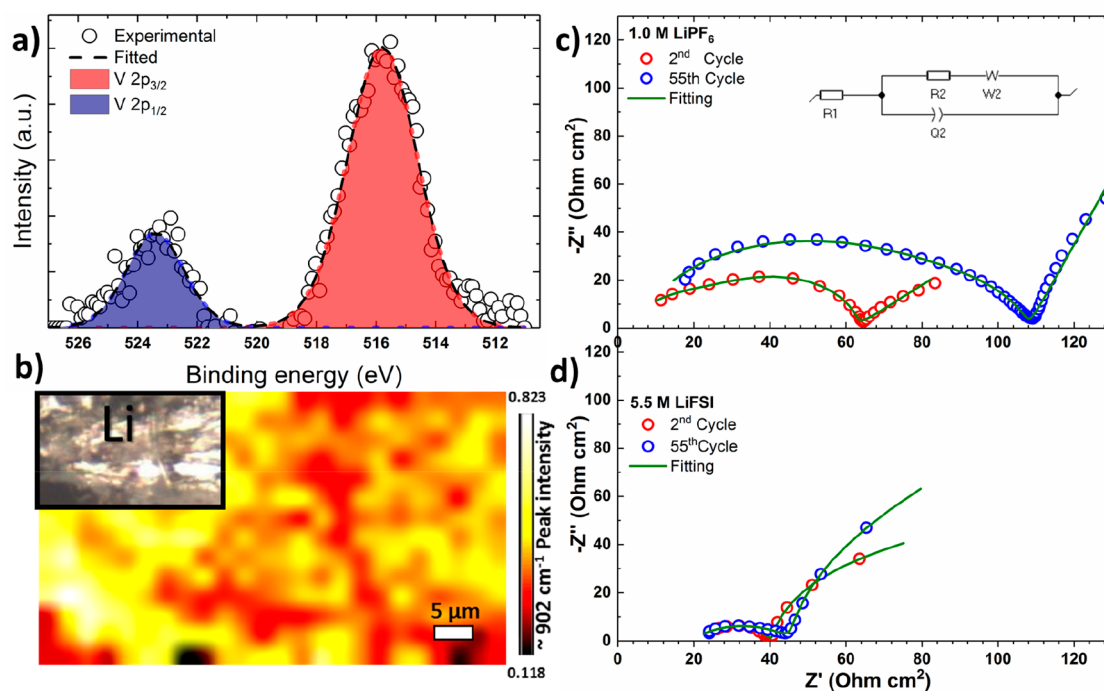
Figure 3. (a) XPS V 2p core level of the vanadium deposited on the anode. (b) Raman mapping of vanadium on the lithium anode. EIS measurements on the positive electrode for different cycles. (c) 1.0M-LiPF$_6$. (d) 5.5M-LiFSI.

209 cut-offs (>4.1 V) and slower cycling, which indicates possible
210 side reactions and instabilities of the electrode−electrolyte
211 interface.[31] In a second attempt, a concentrated 5.5 M lithium
212 bis(fluorosulfonyl) imide (LiFSI) in dimethyl carbonate
213 electrolyte[32] was examined and compared to a conventional
214 1.0 M LiPF$_6$ in ethylene carbonate and dimethyl carbonate
215 (1:1 w/w) electrolyte. Hereafter we will use the notation
216 5.5M-LiFSI and 1.0M-LiPF$_6$, respectively. The cycling stability
217 has been studied at a specific current of 100 mA g^{-1} in the
218 cycling window between 4.1 and 1.3 V, as shown in Figure 2e.
219 Common for both electrolytes is the high first cycle
220 irreversibility. For the cells with 5.5M-LiFSI, the cycling
221 stability increased significantly, exhibiting a specific capacity of
222 155 mAh g^{-1} after 200 cycles compared to the cells with 1.0M-
223 LiPF$_6$ electrolyte exhibiting only 30 mAh g^{-1}. Figure 2f
224 illustrates the rate performance with both electrolytes, which
225 involved five consecutive cycles at a constant specific current at
226 20, 50, 100, 200, 400, and 800 mA g^{-1}. The cells with 1.0M-
227 LiPF$_6$ exhibited a capacity of 345, 302, 275, 248, 208, and 117
228 mAh g^{-1} for the respective second cycle. For 5.5M-LiFSI, the
229 corresponding values were 364, 349, 321, 289, 249, and 190
230 mAh g^{-1}. For higher cycle numbers, the discharge capacity
231 diverges more due to comparably higher capacity fading of the
232 cells with 1.0M-LiPF$_6$ electrolyte. Figures 2g,h show the
233 charge−discharge profile of the second cycle of each current
234 range from the rate-capability test. The molar ratios of solvent
235 and salt of both electrolytes have to be considered to
236 understand the cause for the differences. The molar ratio of
237 solvent to salt corresponds to 13.6:1 for 1M-LiPF$_6$ and 2.7:1
238 for 5.5M-LiFSI, which gives rise to different coordination and
239 solvation of the ions. For the concentrated electrolyte, the ions
240 are expected to form mostly contact ion pairs and aggregated
241 solvate clusters, which can explain the relatively higher
242 viscosity and can lead to a decrease in the ionic
243 conductivity.[25,33] Surprisingly, the rate capabilities are

244 comparable for both electrolytes, which can principally be
245 attributed to the improved electrolyte stability in terms of
246 reduced solvent (unsolvated) availability and possible
247 sacrificial anion reduction, which is hypothesized to lead to
248 lowered interfacial resistances.

Degradation Mechanism: Electrode−Electrolyte In-
250 **teractions.** The results highlight the importance of the
251 optimized electrolyte on the cycling stability of Li$_{2-x}$VO$_2$F. It is
252 generally accepted that all positive electrode materials react
253 with the commonly used electrolytes, which leads to possible
254 passivation.[31] Complementary investigations were carried out
255 with a focus on the electrode−electrolyte interactions at the
256 positive electrode. The lithium electrode of an aged cell was
257 investigated by X-ray photoelectron spectroscopy (XPS) and
258 Raman spectroscopy. XPS was used to probe the oxidation
259 state of the deposited vanadium on the lithium anode surface;
260 the V 2p core level is shown in Figure 3a. The deconvolution
261 of vanadium gives the V 2p$_{3/2}$ peak at 516.1 eV and the V 2p$_{1/2}$
262 peak at 523.5 eV, respectively, and indicates the +4 valence
263 state of vanadium.[34] Furthermore, a surface mapping of
264 vanadium on cycled Li has been done by Raman spectroscopy.
265 It should be noted that Raman spectra are very sensitive to
266 crystal symmetry, coordination geometry, and oxidation states,
267 which make a profound analysis difficult. In the current study,
268 we used Raman only to map the vanadium deposits on the
269 lithium anode. Figure S2 shows the Raman spectra of a cycled
270 Li surface together with the V$_2$O$_5$ reference spectra. The
271 spectra illustrate the deposition of an amorphous VO$_x$-like film
272 on the cycled lithium surface, with the majority of vanadium in
273 the V^{+4} oxidation state. This observation is in accordance with
274 the XPS results. Figure 3b shows the Raman mapping of
275 vanadium on the cycled Li surface using the intensity of the
276 vanadium ∼ 900 cm^{-1} peak, which is the most intense peak
277 and mainly originates due to the stretching vibration of the
278 vanadyl bonds.[35,36]

E

In order to understand the origins of the performance improvements for $Li_{2-x}VO_2F$, electrochemical impedance spectroscopy (EIS) analysis was performed on cycled cells. Furthermore, vanadium dissolution was qualitatively probed for both electrolytes. EIS was measured for the positive electrode at the discharged state after the first formation cycle and the 50th cycle using a three-electrode cell set up at 25 °C. The Nyquist plots for the positive electrode with $1.0M-LiPF_6$ and $5.5M-LiFSI$ are shown in Figure 3, respectively. The Nyquist plots show a semicircle, at the high-frequency region, which can be attributed to the surface film resistance (R1) and the charge transfer resistance (R2) as shown in the fitted circuit. R1 originates from the bulk electrode resistance, and electrolyte resistance R2 is due to the charge transfer resistance at the electrode−electrolyte interface. The Warburg line is attributed to the diffusion of the Li^+-ions to the bulk phase (Warburg element). R1 resistances for $1.0M-LiPF_6$ after the second cycle and 50th cycle were 4.1 Ω cm^2 and 6.6 Ω cm^2, respectively. The corresponding R1 values for $5.5M-LiFSI$ were 22.1 Ω cm^2 and 20.9 Ω cm^2, respectively. The relatively larger R1 values for $5.5M-LiFSI$ could be due to the high viscosity of concentrated electrolyte or as a result of a more dense surface film due to the decomposition of LiFSI salt. The charge transfer resistances R2 for $1.0M-LiPF_6$ after the second cycle and 50th cycle were 30.5 Ω cm^2 and 99.2 Ω cm^2, respectively. The corresponding R2 values for $5.5M-LiFSI$ were 17.3 Ω cm^2 and 23.9 Ω cm^2, respectively. Remarkably, unlike the significant increase of the charge-transfer resistance by ∼225% for cells with $1.0 M-LiPF_6$, the resistances of cells with $5.5M-LiFSI$ increased only slightly by ∼38%. The lower charge-transfer resistance could be due to the formation of a more conductive and stable passivation layer at the cathode−electrolyte interface.[37,38] Furthermore, we argue that in the case of the concentrated electrolyte, dissolution and migration of transition metal can be suppressed due to the lower quantity of unsolvated solvent molecules. The use of concentrated electrolytes with LiFSI can, therefore, increase the cycle life of $Li_{2-x}VO_2F$.

For the dissolution study, VO_2F and nominal "$Li_{1.7}VO_2F$" have been immersed in both electrolytes for 7 days at 45 °C with an electrolyte to electrode material ratio of 50 g/L. Afterward, the amount of vanadium in the electrolyte was determined by inductively coupled plasma-optical emission spectrometry (ICP-OES), and the results are summarized in Table 1. This study gives a clear indication of vanadium dissolution from the positive electrode into the carbonate electrolytes. The pristine VO_2F shows a ∼20 times higher solubility as compared to the lithiated compound in conventional $1.0M-LiPF_6$ electrolyte. It was found that vanadium dissolution is reduced in the concentrated 5.5M-

LiFSI electrolyte showing 3 times lower solubility as compared to $1.0 M-LiPF_6$.

In order to correlate the quantity between deposited V on the anode and the capacity loss, cells have been cycled between 4.5 and 1.3 V at a specific current of 100 mAh g^{-1} and collected after 50 cycles, and the values are given in Table 1. After 50 cycles $Li_{2-x}VO_2F$ cycled with 5.5 M LiFSI and 1.0M-$LiPF_6$ exhibited a discharge capacity of 277 mAh g^{-1} and 199 mAh g^{-1} corresponding to 63% and 50% of the initial capacity, respectively. The loss of capacity due to active material loss is significantly smaller <2% as the total capacity loss based on the measured specific capacity. Interestingly, vanadium dissolution for the cycled cells is ∼6 times lower for the concentrated electrolyte. The active material loss cannot account for the capacity fading but could lead to increased interfacial reactivity and catalytic decomposition of the electrolyte, which could increase capacity fading.[39] The discrepancy in the ratios determined for both methods can be due to higher electrolyte reactivity at 45 °C, different contact times with the electrolyte, varying state of charge influencing the dissolution rate, and possibly differences in the cathode−electrolyte interface, which changes with cycling.[40] The deposited vanadium was found predominantly in the +4 oxidation states, and the dissolution was enhanced for the pristine state with the oxidation state +5; we argue that higher oxidized vanadium is more soluble in carbonate electrolytes. The values we derived must be viewed with caution as we used elevated temperatures and higher active material to electrolyte ratio as compared to test cells, which can increase dissolution but qualitatively gives the right trend. Combining the ICP-OES results and the impedance measurements, we clearly demonstrate that the concentrated LiFSI electrolyte approach was effective in lowering the positive electrode material resistance and in suppressing V dissolution. As a consequence, the cycling performance was improved significantly, but the capacity fading is still pronounced. Although nanosized material is favorable in terms of kinetics offered, it possibly can promote the surface reactivity with the electrolyte due to increased surface area. A detailed mechanistic understanding of the degradation mechanism on the recently discovered Li-rich disordered rock-salts is missing. In the literature performance degradation has been directly correlated with oxygen redox/loss and the associated surface-densification.[41,42] Furthermore, surface-densification can lead to the loss of the lithium-excess, disturbing the lithium percolation and impeding the Li diffusion.[18]

Reaction Mechanism. In order to elucidate the charge compensation mechanism for $Li_{2-x}VO_2F$, we measured V K-edge XANES for different states of charge, as shown in Figures 4a, b. The comparison of the V K-edge for VO_2F with V_2O_5 reference confirms the oxidation state to be V^{+5}. VO_2F shows a weak pre-edge peak located at 5469 eV, which originates from the transition to 3d states of vanadium hybridized with 4p in the distorted octahedral environment.[43] Upon discharge (lithiation) from OCV (pristine state) to 1.3 V, the absorption edge shifts to lower energies, close to the position of the reference compound Li_2VO_2F with V^{+3} as shown in Figure 4a. This trend agrees with the observed discharge capacity, corresponding to 1.7 Li per f.u. and an oxidation state of ∼3.3. With deviation from octahedral symmetry, pre-edge peak intensity typically increases. Furthermore, it depends on the number of d-electrons and is maximized for the d^0-configuration.[43] The increase of the pre-edge intensity after

Table 1. Dissolution of Vanadium in the Electrolyte at 45 °C for the Pristine and Discharged States

Compounds	V dissolution %	
	1.0 M LiPF$_6$	5.5 M LiFSI
VO_2F	4.49 ± 0.13	1.55 ± 0.04
$Li_{1.7}VO_2F$	0.22 ± 0.01	0.02 ± 0.01
$Li_{2-x}VO_2F$	[a]3.51 ± 0.04	[b]1.15 ± 0.03
V concentration on Li Anode after 50 cycles		
$Li_{2-x}VO_2F$	1.8 ± 0.10	0.30 ± 0.05

[a] x = 1.37. [b] x = 1.45 and vanadium deposit on anode after 50 cycles.

a)

b)

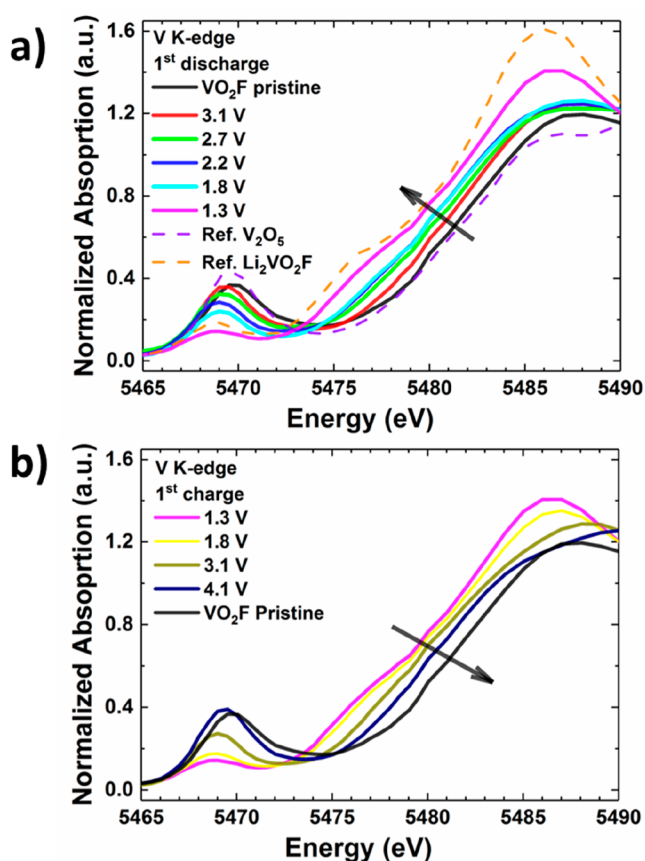**Figure 4.** (a) V K-edge XANES for $Li_{2-x}VO_2F$ measured at different voltages for the first discharge starting from OCV to 1.3 V. (b) V K-edge XANES measured at different voltages for the first charge.

discharge indicates a structural distortion. Upon charging, the V absorption edge shifts to higher energy values but does not recover to the edge position of the pristine V^{+5} state, as shown in Figure 4b. This observation is in accordance with the first cycle irreversibility. Recently, the first cycle irreversibility in cation-disordered oxyfluoride systems has been rationalized by the Ceder group[8,44] with the lithium-gettering effect introduced by fluorine (Li-rich sites around F), preferentially becoming undercoordinated for high delithiation degrees, which results in a stronger bond between Li−F and necessitates higher extraction voltages for these Li^+-ions.

In-situ differential electrochemical mass spectrometry (DEMS) measurements were conducted for Li_2VO_2F. The upper cutoff voltage was varied from 4.5 V in the first cycle to 4.8 V for the second and third cycles. Figure S3 compares the potential and gas evolution profiles for the first three cycles. CO_2 evolution started at 3.6 V and increases along with the potential and can be attributed to the electrochemical electrolyte oxidation.[45,46] For the second cycle with the higher cutoff, CO evolution was observed at 4.7 V, which can possibly be attributed to the oxidation of conductive carbon.[47]

Summary. In summary, we have investigated the failure mechanism of $Li_{2-x}VO_2F$ from the perspective of the cathode−electrolyte interactions. The cycling stability significantly improved by using a concentrated electrolyte with 5.5 M LiFSI in DMC. Vanadium dissolution is a critical issue and can be suppressed with concentrated electrolytes. In particular, the lowered vanadium solubility and the reduced interfacial resistances were found to increase the cycling stability. The

capacity loss due to the active material loss through dissolution is considerably smaller than the total capacity fading. Therefore, improvement in cycling stability can be attributed to improved cathode−electrolyte interactions. Yet, the cycling stability continuously decreases and hints toward other degradation mechanisms. V K-edge XANES results show that charge-compensation is associated with V^{3+}/V^{5+} redox reaction accounting for the measured reversible capacity. The reoxidation to V^{+5} is incomplete and leads to high first cycle irreversibility. Furthermore, we demonstrated the feasibility to synthesize Li_2VO_2F by chemical lithiation of VO_2F with *n*-BuLi. We propose vanadium dissolution and interfacial reactivity as an additional constraint for the realization of vanadium-based disordered rock-salts with high cycling stability. The presented findings are expected to benefit other systems containing transition metals prone to dissolution.

■ EXPERIMENTAL SECTION

Synthesis. *VO₂F.* The synthesis procedure was adapted from our previous work.[13] Stoichiometric amounts of V_2O_5 and VOF_3 were milled with 600 rpm for 20 h using a Fritsch P6 planetary ball mill with an 80 mL silicon nitride vial and silicon nitride ball with a ball to powder ratio of 15:1.

Li₂VO₂F. Chemical lithiation was carried out in a Schlenk tube under argon atmosphere in a cold bath of dry ice/acetone mixture (−78 °C). To a suspension of VO_2F in dry hexane was added at once 2.1 equiv of *n*-butyllithium (2.5 M in hexane). The suspension was stirred overnight. For complete lithiation, the suspension was heated to 50 °C and stirred for 2 more days and then filtrated and washed several times with hexane.

5.5M-LiFSI electrolyte: LiFSI (Nippon Shokubai) and DMC (BASF) with battery grade. Electrolyte solutions were prepared by mixing the appropriate quantity of LiFSI and the solvent (5.5 mol LiFSI in 1L DMC). The obtained electrolyte was a clear solution.

Electrochemical Measurements. Electrochemical tests were carried out in Swagelok-type cell using lithium as a counter electrode. Electrode slurries were made of 90 wt % composite and 10 wt % polyvinylidene difluoride (PVDF) binder with *N*-methyl-2-pyrrolidone (NMP) as a solvent. The composite consists of active material and Super C65 carbon black in a weight ratio of 80:20. The mixed slurry was coated on an aluminum foil by a doctor blade technique and dried at 120 °C for 12 h under vacuum. Each working electrode (12 mm diameter) contained approximately 3 mg of active material, and Li foil was used as a counter electrode. LP30 from BASF (ethylene carbonate/dimethyl carbonate, 1:1 weight ratio with 1 M $LiPF_6$) was used as the electrolyte. Temperature controlled galvanostatic charge−discharge experiments were conducted at 25 °C in climate chambers using an Arbin electrochemical workstation.

Electrochemical impedance spectroscopy (EIS) was performed using a three-electrode PAT-Cell (EL-CELL, Germany) with Li ring as reference electrode and Li metal (18 mm) as the counter electrode. The working electrode size was 18 mm and aluminum as the current collector. The experiments were conducted using a Bio-Logic electrochemical workstation with an applied sinusoidal excitation voltage of 10 mV in the frequency range 200 kHz−0.1 Hz.

Differential Electrochemical Mass Spectrometry (DEMS). The in situ gas analysis was performed by use of differential electrochemical mass spectrometry (DEMS). The setup has been described elsewhere.[46,48] Custom cells with gas in- and outlets were assembled in an argon-filled glovebox. The cathodes used were 40 mm diameter with a 4 mm hole for proper gas extraction. GF/A (42 mm diameter, GE Healthcare Life Sciences, Whatman) was used as separator, 600 μL of LP47 (1 M $LiPF_6$ in ethylene carbonate/diethyl carbonate, 3:7 by weight, BASF SE) as electrolyte, and 600 μm-thick Li metal foil (Albemarle Germany GmbH) with a diameter of 40 mm as counter-electrode. A constant carrier gas flow (2.5 mL_{He}/min, purity 6.0) was applied during DEMS measurements for gas

extraction. The gas was analyzed via mass spectrometry (GSD 320, OmniStar Gas Analysis System, Pfeiffer Vacuum GmbH). After each run, a calibration gas of known composition was introduced to quantify the measured ion currents.

X-ray Diffraction. Synchrotron X-ray powder diffraction (XRPD) experiments were performed at the Swiss-Norwegian Beamline (SNBL), beamline BM01, at the European Synchrotron Radiation Facility (ESRF). The powdered samples were filled in 0.5 mm quartz capillaries and sealed with wax under an argon atmosphere. XRPD data were collected using a PILATUS 2 M area detector from DECTRIS, a sample-to-detector distance of 142.27 mm, beam size of 0.2×0.2 mm, a wavelength of 0.68202 Å, a 20° rotation of the capillary, and an exposure time of 20 s. The data were converted to conventional one-dimensional powder patterns using the FIT2D software.[49] The electrochemically lithiated $Li_{2-x}VO_2F$ powder sample was sealed in between polyimide foil under an argon atmosphere. Powder diffraction data was recorded on a HUBER diffractometer with a RIGAKU micro focus rotating-anode (Mo Kα1,2 radiation), a 2D collimating multilayer optic, and a PILATUS 300 K-W detector. The area detector data were converted to one-dimensional powder patterns using the pyFAI software.[50]

Raman. Raman measurements of the surface of cycled Lithium were conducted using an ECC-Opto-Std [EL-CELL GmbH] electrochemical cell. The washed lithium after battery cycling was kept at the electrode side of an ECC-Opto-Std [EL-CELL GmbH] cell and sealed with a thin optical glass window (0.15 mm) and made airtight with a rubber seal. The whole cell was fabricated inside a glovebox. The Raman spectra and mapping were acquired using an inVia confocal Raman microscope (RENISHAW) with a 532 nm laser excitation source in the spectral range $600-1000$ cm^{-1}. A grating was used as a dispersion element with a groove density of 2400 l/mm. The slit opening of the confocal system was fixed at 65 μm and centered at 1859 μm, respectively. The laser was focused on the sample using a 20× objective. The nominal laser power was filtered down to 4 mW to avoid sample overheating. Every spectrum recorded resulted from an average of 2 acquisitions of 5 s each. The data were analyzed using inVia *WiRE 4.4 Software*.

TEM. High-resolution transmission electron microscopy (HRTEM) imaging was performed on a Titan 80-300 TEM equipped with an objective lens spherical aberration (Cs) corrector and operated at 80 kV. EELS spectra were acquired using a Gatan-Tridiem spectrometer attached to the TEM. The energy resolution was determined to be 0.60 eV. Short exposure times in the order of $0.05-0.1$ s were used during the acquisition of the spectrum. The spectra were corrected for multiple scattering by using the Fourier-log deconvolution method. For the O$-$K V L$_{2,3}$ and F$-$K edges, the acquisition times were in the order of 5 s. The background contribution at the F$-$K, O$-$K edge, and V L$_{2,3}$ edges was subtracted after fitting of the background using a power law AE$-$r, with E being the energy loss and A and r being constants. In order to remove the effects of the multiple scattering, core-loss spectra were deconvoluted with the low loss spectrum.

XANES. The V K-edge XANES spectra were measured with a laboratory Rigaku R-XAS spectrometer (Southern Federal University, Russia) in transmission mode at room temperature with a crystal monochromator Ge (311) at an energy resolution of 0.6 eV. The material was extracted from the electrochemical cell at different voltages and pressed into pellets. The latter was prepared in a glovebox and sealed in a transparent X-ray bag under an inert atmosphere for measurements. An argon-filled ionization chamber (300 mbar pressure) was used to detect the intensity of the incoming X-ray radiation, and a scintillation counter was used for the transmitted intensity. The goniometer section of the spectrometer was filled with helium buffer gas to avoid the air absorption of X-rays. Ten spectra were acquired and averaged for each sample.

■ ASSOCIATED CONTENT

ⓢ Supporting Information

The Supporting Information is available free of charge on the ACS Publications website at DOI: 10.1021/acs.chemmater.9b02074.

> Additional XRPD and Rietveld refinement results for the intermediate phases of $Li_{2-x}VO_2F$ with 12 h immersion in *n*-BuLi. Structural parameters for the intermediate phases. Raman spectra of cycled lithium anode. DEMS measurement for Li_2VO_2F (PDF)

■ AUTHOR INFORMATION

Corresponding Author

*E-mail: m.fichtner@kit.edu.

ORCID ⓘ

Musa Ali Cambaz: 0000-0002-4249-3486
Bhaghavathi P. Vinayan: 0000-0001-6491-5160
Syed Atif Pervez: 0000-0002-7134-7103

Notes

The authors declare no competing financial interest.

■ REFERENCES

(1) Myung, S.-T.; Maglia, F.; Park, K.-J.; Yoon, C. S.; Lamp, P.; Kim, S.-J.; Sun, Y.-K. Nickel-Rich Layered Cathode Materials for Automotive Lithium-Ion Batteries: Achievements and Perspectives. *ACS Energy Lett.* 2017, 2 (1), 196−223.

(2) Etacheri, V.; Marom, R.; Elazari, R.; Salitra, G.; Aurbach, D. Challenges in the Development of Advanced Li-Ion Batteries: A Review. *Energy Environ. Sci.* 2011, 4 (9), 3243.

(3) Scrosati, B.; Hassoun, J.; Sun, Y.-K. Lithium-Ion Batteries. A Look into the Future. *Energy Environ. Sci.* 2011, 4 (9), 3287.

(4) Lee, J.; Urban, A.; Li, X.; Su, D.; Hautier, G.; Ceder, G. Unlocking the Potential of Cation-Disordered Oxides for Rechargeable Lithium Batteries. *Science (Washington, DC, U. S.)* 2014, 343 (6170), 519−522.

(5) Yabuuchi, N.; Takeuchi, M.; Nakayama, M.; Shiiba, H.; Ogawa, M.; Nakayama, K.; Ohta, T.; Endo, D.; Ozaki, T.; Inamasu, T.; et al. High-Capacity Electrode Materials for Rechargeable Lithium Batteries: Li3NbO4 -Based System with Cation-Disordered Rocksalt Structure. *Proc. Natl. Acad. Sci. U. S. A.* 2015, 112 (25), 7650−7655.

(6) Lee, J.; Seo, D.-H.; Balasubramanian, M.; Twu, N.; Li, X.; Ceder, G. A New Class of High Capacity Cation-Disordered Oxides for Rechargeable Lithium Batteries: Li−Ni−Ti−Mo Oxides. *Energy Environ. Sci.* 2015, 8 (11), 3255−3265.

(7) Hoshino, S.; Glushenkov, A. M.; Ichikawa, S.; Ozaki, T.; Inamasu, T.; Yabuuchi, N. Reversible Three-Electron Redox Reaction

of Mo 3+ /Mo 6+ for Rechargeable Lithium Batteries. *ACS Energy Lett.* **2017**, *2* (4), 733−738.

(8) Kitchaev, D. A.; Lun, Z.; Richards, W. D.; Ji, H.; Clément, R. J.; Balasubramanian, M.; Kwon, D.-H.; Dai, K.; Papp, J. K.; Lei, T.; et al. Design Principles for High Transition Metal Capacity in Disordered Rocksalt Li-Ion Cathodes. *Energy Environ. Sci.* **2018**, *11* (8), 2159−2171.

(9) KITAJOU, A.; TANAKA, K.; MIKI, H.; KOGA, H.; OKAJIMA, T.; OKADA, S. Improvement of Cathode Properties by Lithium Excess in Disordered Rocksalt Li2 + 2xMn1−xTi1−xO4. *Electrochemistry* **2016**, *84* (8), 597−600.

(10) Cambaz, M. A.; Vinayan, B. P.; Euchner, H.; Johnsen, R. E.; Guda, A. A.; Mazilkin, A.; Rusalev, Y. V.; Trigub, A. L.; Gross, A.; Fichtner, M. Design of Nickel-Based Cation-Disordered Rock-Salt Oxides: The Effect of Transition Metal (M = V, Ti, Zr) Substitution in LiNi 0.5 M 0.5 O 2 Binary Systems. *ACS Appl. Mater. Interfaces* **2018**, *10* (26), 21957−21964.

(11) Twu, N.; Li, X.; Urban, A.; Balasubramanian, M.; Lee, J.; Liu, L.; Ceder, G. Designing New Lithium-Excess Cathode Materials from Percolation Theory: Nanohighways in Li x Ni 2−4 x /3 Sb x /3 O 2. *Nano Lett.* **2015**, *15* (1), 596−602.

(12) Nakajima, M.; Yabuuchi, N. Lithium-Excess Cation-Disordered Rocksalt-Type Oxide with Nanoscale Phase Segregation: Li$_{1.25}$Nb$_{0.25}$V$_{0.5}$O$_2$. *Chem. Mater.* **2017**, *29* (16), 6927−6935.

(13) Cambaz, M. A.; Vinayan, B. P.; Clemens, O.; Munnangi, A. R.; Chakravadhanula, V. S. K.; Kübel, C.; Fichtner, M. Vanadium Oxyfluoride/Few-Layer Graphene Composite as a High-Performance Cathode Material for Lithium Batteries. *Inorg. Chem.* **2016**, *55* (8), 3789−3796.

(14) Chen, R.; Ren, S.; Knapp, M.; Wang, D.; Witter, R.; Fichtner, M.; Hahn, H. Disordered Lithium-Rich Oxyfluoride as a Stable Host for Enhanced Li + Intercalation Storage. *Adv. Energy Mater.* **2015**, *5* (9), 1401814.

(15) Ren, S.; Chen, R.; Maawad, E.; Dolotko, O.; Guda, A. A.; Shapovalov, V.; Wang, D.; Hahn, H.; Fichtner, M. Improved Voltage and Cycling for Li + Intercalation in High-Capacity Disordered Oxyfluoride Cathodes. *Adv. Sci.* **2015**, *2* (10), 1500128.

(16) Hoshino, S.; Glushenkov, A. M.; Ichikawa, S.; Ozaki, T.; Inamasu, T.; Yabuuchi, N. Reversible Three-Electron Redox Reaction of Mo 3+ /Mo 6+ for Rechargeable Lithium Batteries. *ACS Energy Lett.* **2017**, *2* (4), 733−738.

(17) Richards, W. D.; Dacek, S. T.; Kitchaev, D. A.; Ceder, G. Fluorination of Lithium-Excess Transition Metal Oxide Cathode Materials. *Adv. Energy Mater.* **2018**, *8* (5), 1701533.

(18) Lee, J.; Papp, J. K.; Clément, R. J.; Sallis, S.; Kwon, D.-H.; Shi, T.; Yang, W.; McCloskey, B. D.; Ceder, G. Mitigating Oxygen Loss to Improve the Cycling Performance of High Capacity Cation-Disordered Cathode Materials. *Nat. Commun.* **2017**, *8* (1), 981.

(19) Wang, X.; Huang, Y.; Ji, D.; Omenya, F.; Karki, K.; Sallis, S.; Piper, L. F. J.; Wiaderek, K. M.; Chapman, K. W.; Chernova, N. A.; et al. Structure Evolution and Thermal Stability of High-Energy-Density Li-Ion Battery Cathode Li $_2$ VO $_2$ F. *J. Electrochem. Soc.* **2017**, *164*, A1552.

(20) Pérez-Flores, J. C.; Villamor, R.; Ávila-Brande, D.; Gallardo Amores, J. M.; Morán, E.; Kuhn, A.; García-Alvarado, F. VO 2 F: A New Transition Metal Oxyfluoride with High Specific Capacity for Li Ion Batteries. *J. Mater. Chem. A* **2015**, *3* (41), 20508−20515.

(21) Chen, R.; Maawad, E.; Knapp, M.; Ren, S.; Beran, P.; Witter, R.; Hempelmann, R. Lithiation-Driven Structural Transition of VO 2 F into Disordered Rock-Salt Li x VO 2 F. *RSC Adv.* **2016**, *6* (69), 65112−65118.

(22) Wang, X.; Lin, Y.-C.; Zhou, H.; Omenya, F.; Chu, I.-H.; Karki, K.; Sallis, S.; Rana, J.; Piper, L. F. J.; Chernova, N. A.; et al. Structural Changes in a High-Energy Density VO 2 F Cathode upon Heating and Li Cycling. *ACS Appl. Energy Mater.* **2018**, *1* (9), 4514−4521.

(23) Zhang, H.; Feng, W.; Nie, J.; Zhou, Z. Recent Progresses on Electrolytes of Fluorosulfonimide Anions for Improving the Performances of Rechargeable Li and Li-Ion Battery. *J. Fluorine Chem.* **2015**, *174*, 49−61.

(24) Eshetu, G. G.; Grugeon, S.; Gachot, G.; Mathiron, D.; Armand, M.; Laruelle, S. LiFSI vs. LiPF6 Electrolytes in Contact with Lithiated Graphite: Comparing Thermal Stabilities and Identification of Specific SEI-Reinforcing Additives. *Electrochim. Acta* **2013**, *102*, 133−141.

(25) Wang, J.; Yamada, Y.; Sodeyama, K.; Chiang, C. H.; Tateyama, Y.; Yamada, A. Superconcentrated Electrolytes for a High-Voltage Lithium-Ion Battery. *Nat. Commun.* **2016**, *7* (1), 12032.

(26) YAMADA, Y. Developing New Functionalities of Super-concentrated Electrolytes for Lithium-Ion Batteries. *Electrochemistry* **2017**, *85* (9), 559−565.

(27) Golden, J. H.; DiSalvo, F. J.; Frechet, J. M. J. Room-Temperature Synthesis of (LiMo3Se3)n and the Determination of the Relative Reduction Potential of Tert-Butyllithium. *Chem. Mater.* **1994**, *6* (6), 844−849.

(28) Cambaz, M. A.; Vinayan, B. P.; Euchner, H.; Johnsen, R. E.; Guda, A. A.; Mazilkin, A.; Rusalev, Y. V.; Trigub, A. L.; Gross, A.; Fichtner, M. Design of Nickel-Based Cation-Disordered Rock-Salt Oxides: The Effect of Transition Metal (M = V, Ti, Zr) Substitution in LiNi0.5M0.5O2 Binary Systems. *ACS Appl. Mater. Interfaces* **2018**, *10* (26), 21957−21964.

(29) Cambaz, M. A.; Vinayan, B. P.; Clemens, O.; Munnangi, A. R.; Chakravadhanula, V. S. K.; Kübel, C.; Fichtner, M. Vanadium Oxyfluoride/Few-Layer Graphene Composite as a High-Performance Cathode Material for Lithium Batteries. *Inorg. Chem.* **2016**, *55* (8), 3789−3796.

(30) Momma, K.; Izumi, F. VESTA 3 for Three-Dimensional Visualization of Crystal, Volumetric and Morphology Data. *J. Appl. Crystallogr.* **2011**, *44* (6), 1272−1276.

(31) Aurbach, D.; Markovsky, B.; Salitra, G.; Markevich, E.; Talyossef, Y.; Koltypin, M.; Nazar, L.; Ellis, B.; Kovacheva, D. Review on Electrode−Electrolyte Solution Interactions, Related to Cathode Materials for Li-Ion Batteries. *J. Power Sources* **2007**, *165* (2), 491−499.

(32) Wang, J.; Yamada, Y.; Sodeyama, K.; Chiang, C. H.; Tateyama, Y.; Yamada, A. Superconcentrated Electrolytes for a High-Voltage Lithium-Ion Battery. *Nat. Commun.* **2016**, *7* (1), 12032.

(33) Qian, J.; Henderson, W. A.; Xu, W.; Bhattacharya, P.; Engelhard, M.; Borodin, O.; Zhang, J.-G. High Rate and Stable Cycling of Lithium Metal Anode. *Nat. Commun.* **2015**, *6* (1), 6362.

(34) Biesinger, M. C.; Lau, L. W. M.; Gerson, A. R.; Smart, R. S. C. Resolving Surface Chemical States in XPS Analysis of First Row Transition Metals, Oxides and Hydroxides: Sc, Ti, V, Cu and Zn. *Appl. Surf. Sci.* **2010**, *257* (3), 887−898.

(35) Lee, S.-H.; Cheong, H. M.; Je Seong, M.; Liu, P.; Tracy, C. E.; Mascarenhas, A.; Pitts, J. R.; Deb, S. K. Microstructure Study of Amorphous Vanadium Oxide Thin Films Using Raman Spectroscopy. *J. Appl. Phys.* **2002**, *92* (4), 1893−1897.

(36) Zhang, C.; Yang, Q.; Koughia, C.; Ye, F.; Sanayei, M.; Wen, S.-J.; Kasap, S. Characterization of Vanadium Oxide Thin Films with Different Stoichiometry Using Raman Spectroscopy. *Thin Solid Films* **2016**, *620*, 64−69.

(37) Yu, X.; Manthiram, A. Electrode−Electrolyte Interfaces in Lithium-Based Batteries. *Energy Environ. Sci.* **2018**, *11* (3), 527−543.

(38) Edström, K.; Gustafsson, T.; Thomas, J. O. The Cathode−Electrolyte Interface in the Li-Ion Battery. *Electrochim. Acta* **2004**, *50* (2−3), 397−403.

(39) Wang, C.; Xing, L.; Vatamanu, J.; Chen, Z.; Lan, G.; Li, W.; Xu, K. Overlooked Electrolyte Destabilization by Manganese (II) in Lithium-Ion Batteries. *Nat. Commun.* **2019**, *10* (1), 3423.

(40) Cabana, J.; Kwon, B. J.; Hu, L. Mechanisms of Degradation and Strategies for the Stabilization of Cathode−Electrolyte Interfaces in Li-Ion Batteries. *Acc. Chem. Res.* **2018**, *51* (2), 299−308.

(41) Chen, D.; Kan, W. H.; Chen, G. Understanding Performance Degradation in Cation-Disordered Rock-Salt Oxide Cathodes. *Adv. Energy Mater.* **2019**, *9* (31), 1901255.

(42) Cambaz, M. A.; Vinayan, B. P.; Geßwein, H.; Schiele, A.; Sarapulova, A.; Diemant, T.; Mazilkin, A.; Brezesinski, T.; Behm, R. J.; Ehrenberg, H.; et al. Oxygen Activity in Li-Rich Disordered Rock-Salt

Oxide and the Influence of LiNbO 3 Surface Modification on the Electrochemical Performance. *Chem. Mater.* **2019**, *31* (12), 4330−4340.

(43) Yamamoto, T. Assignment of Pre-Edge Peaks in K-Edge x-Ray Absorption Spectra of 3d Transition Metal Compounds: Electric Dipole or Quadrupole? *X-Ray Spectrom.* **2008**, *37* (6), 572−584.

(44) Clément, R. J.; Kitchaev, D.; Lee, J.; Gerbrand, C. Short-Range Order and Unusual Modes of Nickel Redox in a Fluorine-Substituted Disordered Rocksalt Oxide Lithium-Ion Cathode. *Chem. Mater.* **2018**, *30* (19), 6945−6956.

(45) Metzger, M.; Strehle, B.; Solchenbach, S.; Gasteiger, H. A. Origin of H2 Evolution in LIBs: H2O Reduction vs. Electrolyte Oxidation. *J. Electrochem. Soc.* **2016**, *163* (5), A798−A809.

(46) Berkes, B. B.; Schiele, A.; Sommer, H.; Brezesinski, T.; Janek, J. On the Gassing Behavior of Lithium-Ion Batteries with NCM523 Cathodes. *J. Solid State Electrochem.* **2016**, *20* (11), 2961−2967.

(47) Metzger, M.; Sicklinger, J.; Haering, D.; Kavakli, C.; Stinner, C.; Marino, C.; Gasteiger, H. A. Carbon Coating Stability on High-Voltage Cathode Materials in H 2 O-Free and H 2 O-Containing Electrolyte. *J. Electrochem. Soc.* **2015**, *162* (7), A1227−A1235.

(48) Berkes, B. B.; Jozwiuk, A.; Vračar, M.; Sommer, H.; Brezesinski, T.; Janek, J. Online Continuous Flow Differential Electrochemical Mass Spectrometry with a Realistic Battery Setup for High-Precision, Long- Term Cycling Tests. *Anal. Chem.* **2015**, *87* (12), 5878−5883.

(49) Hammersley, A. P.; Svensson, S. O.; Hanfland, M.; Fitch, A. N.; Hausermann, D. Two-Dimensional Detector Software: From Real Detector to Idealised Image or Two-Theta Scan. *High Pressure Res.* **1996**, *14* (4−6), 235−248.

(50) Ashiotis, G.; Deschildre, A.; Nawaz, Z.; Wright, J. P.; Karkoulis, D.; Picca, F. E.; Kieffer, J. The Fast Azimuthal Integration Python Library: PyFAI. *J. Appl. Crystallogr.* **2015**, *48* (2), 510−519.